Research Square

Preprints are preliminary reports that have not undergone peer review.
They should not be considered conclusive, used to inform clinical practice,
or referenced by the media as validated information.

Visualization of elastic fibres with Evans Blue during organ maturation, homeostasis and across aging

Yojiro Yamanaka

yojiro.yamanaka@mcgill.ca

McGill

Warwick Pitman

McGill https://orcid.org/0009-0008-4998-5310

Kerstin Tiedemann

McGill

Alexandra Segal

McGill

Alexandra Viscotchi

McGill https://orcid.org/0009-0008-3920-9529

Katie Cockburn

McGill

Dieter Reinhardt

McGill University https://orcid.org/0000-0001-6535-9872

Article

Keywords:

Posted Date: November 26th, 2026

DOI: https://doi.org/10.21203/rs.3.rs-11485352/v1

License: This work is licensed under a Creative Commons Attribution 4.0 International License.
Read Full License

Additional Declarations:
There is **NO** Competing Interest.

All animal-related procedures were approved by the McGill Animal Care Committee under AUP7843.

Title: Visualization of elastic fibres with Evans Blue during organ maturation, homeostasis and across aging.

Warwick Pitman[1], Kerstin Tiedemann[2], Alexandra Segal[1], Alexandra Viscotchi[1], Katie Cockburn[3], Dieter P. Reinhardt[2,4], Yojiro Yamanaka[1,#].

[1]Rosalind and Morris Goodman Cancer Research Institute, Department of Human Genetics, McGill University, Montreal, QC H3A 1A3, Canada.

[2]Faculty of Medicine and Health Sciences, Department of Anatomy and Cell Biology, McGill University, Montreal, QC, Canada.

[3]Rosalind and Morris Goodman Cancer Research Institute, Department of Biochemistry, McGill University, Montreal, QC H3A 1A3, Canada.

[4]Faculty of Dental Medicine and Oral Health Sciences, McGill University, Montreal, QC, Canada.

#Corresponding author email: Yojiro.yamanaka@mcgill.ca

Key words: Elastic fibres, Elasticity, 3D microscopy, ECM, Organ maturation, Homeostasis, Aging

Abstract:

Elasticity is an essential biophysical property of animal tissues. Elastin, the core component of elastic fibres, is predominantly deposited early in life and undergoes little-to-no turnover thereafter, despite its progressive loss with aging. Although tissue elasticity is required throughout organ maturation, homeostasis, and aging, three-dimensional visualization of elastic fibres within wholemount tissue remains challenging. Here, we demonstrate that Evans Blue, an inexpensive and well-

characterized intravital dye, can be used to fluorescently label elastic fibres in live, fixed, and cleared whole-mount tissues. Using this approach, we reveal widespread elastic fibre networks within the sub-mesothelial layer of visceral organs and demonstrate that their density and organization vary across organs and life stages. Together, these findings establish Evans Blue as a simple and readily adoptable method for three-dimensional visualization of elastic fibres and provide a framework for investigating how elastic fibre architecture supports organ structure during development and homeostasis, and how its deterioration may contribute to age-associated functional decline.

Introduction:

The biophysical properties of visceral internal organs are supported by the extracellular matrix (ECM), which maintains consistent organ shape and elasticity by providing sufficient control over tissue structure and function, under homeostatic conditions. Membranous ECM, lining the basal side of epithelia and endothelium, physically separate tissue from the surrounding interstitium. On the other hand, fibrous ECM, a mesh-like group of fibres, collectively act to confer each organ with a unique structural framework for cells to live and move within[1,2]. The meshwork of fibrous ECM includes, but is not limited to, collagen and elastic fibres, which provide each organ with a degree of tensile strength and elasticity, respectively. Interestingly, elastin, the core component of elastic fibres, is suggested to only be deposited during development and the neonatal period, contrasting with collagen, which is deposited throughout an individual's lifespan[3]. Critically, the excess deposition of collagen, instead of elastin,

during wound healing and/or the aging process, is thought to confer tissue with a sclerotic (stiffened) phenotype[4,5].

Evans blue (EB) is a dye that has been commonly used for decades to study plasma permeability, most famously within the brain to aid investigating the integrity of the blood-brain barrier (BBB)[6,7]. This is primarily due to the dye's ability to bind to albumin, and its strong blue colour providing a gross reference for plasma leakage. In addition to its innate blue colour, EB gains fluorescence in the far-red spectrum after binding to albumin[8,9]. This property is highly useful for fluorescent microscopy analysis, as it provides a method to label intact vasculature across organ systems[10,11]. On the other hand, skepticism regarding EB's efficacy to study the BBB has remained within the field[7]. Traditional studies, although often overlooked, suggest that a measurable amount of free EB dye exists following perfusion[12,13], and that EB carries a capacity to bind to tissue components[14,15].

Whilst utilizing EB to label albumin across murine organs to aid visualizing the vascular system, we serendipitously observed fibrous fluorescence within the interstitium. This was reproducible across different experimental strategies and methods of tissue preparation, such as live, fixed and/or cleared contexts, following EB perfusion and/or through direct immersion with the dye *in vitro*. To our surprise, the EB+ fibrous structures were found to be elastic fibres. We demonstrated this by showing that EB becomes fluorescent after binding to purified elastin and by co-staining patterns with fibrillin-1 and tropoelastin immunostaining. Thus, we envision that EB, an inexpensive and well-studied intravital dye, could be of great utility in elucidating the role of elasticity in tissue physiological functioning, during development and homeostasis, and

how its loss during the aging process contributes as the key modulator of sclerosis across aged tissue.

Results:

Evans Blue fluorescently labels fibrous structures below the mesothelial surface of visceral organs.

Considering that fluid exchange aids regulating tissue homeostasis through the delivery of oxygen and nutrients, we aimed to track plasma permeability between the capillaries and organ interstitium, using EB dye. Consistent with previous studies, the visible blue colour of EB aided us in grossly tracking vascular patterns and plasma permeability across murine organs. Macroscopically, the brain, fat, lungs, abdominal wall and seminal vesicles remained white in colour, whilst other organs exhibited differing degrees of blueness, illustrating the distinct physiological state of EB capillary extravasation across murine organs (Fig 1B). In addition, as previously described[6], perfusion of EB was able to illustrate the integrity of the blood brain barrier, whereby EB remained within vasculature of the brain, whilst within other murine organs, such as the pancreas, EB extravasated into the interstitium (Fig 1C).

In addition to the visible blue colour that grossly visualized EB permeability patterns, EB far-red fluorescence, upon albumin binding, has enabled assessment of the plasma proteins leakage across organ systems. Apart from the spleen, at low magnification, we generally observed that EB fluorescence localized within the lumen of Flk1GFP+ (VEGFR2+) endothelial cells across murine organs (Fig 1D). However, at high

magnification, we identified that EB fluorescence reproducibly labelled fibrous structures near the tissue surface (Fig 1E). As we imaged deeper into each organ's parenchyma, EB was found to fluorescently label the plasma within the lumen of Flk1GFP+ capillaries (Fig 1E). The spleen showed unique patterns, whereby no EB was found within the vascular lumen, despite fibrous structures near the tissue surface being robustly labelled (Fig 1E), likely reflecting its open capillary system[16].

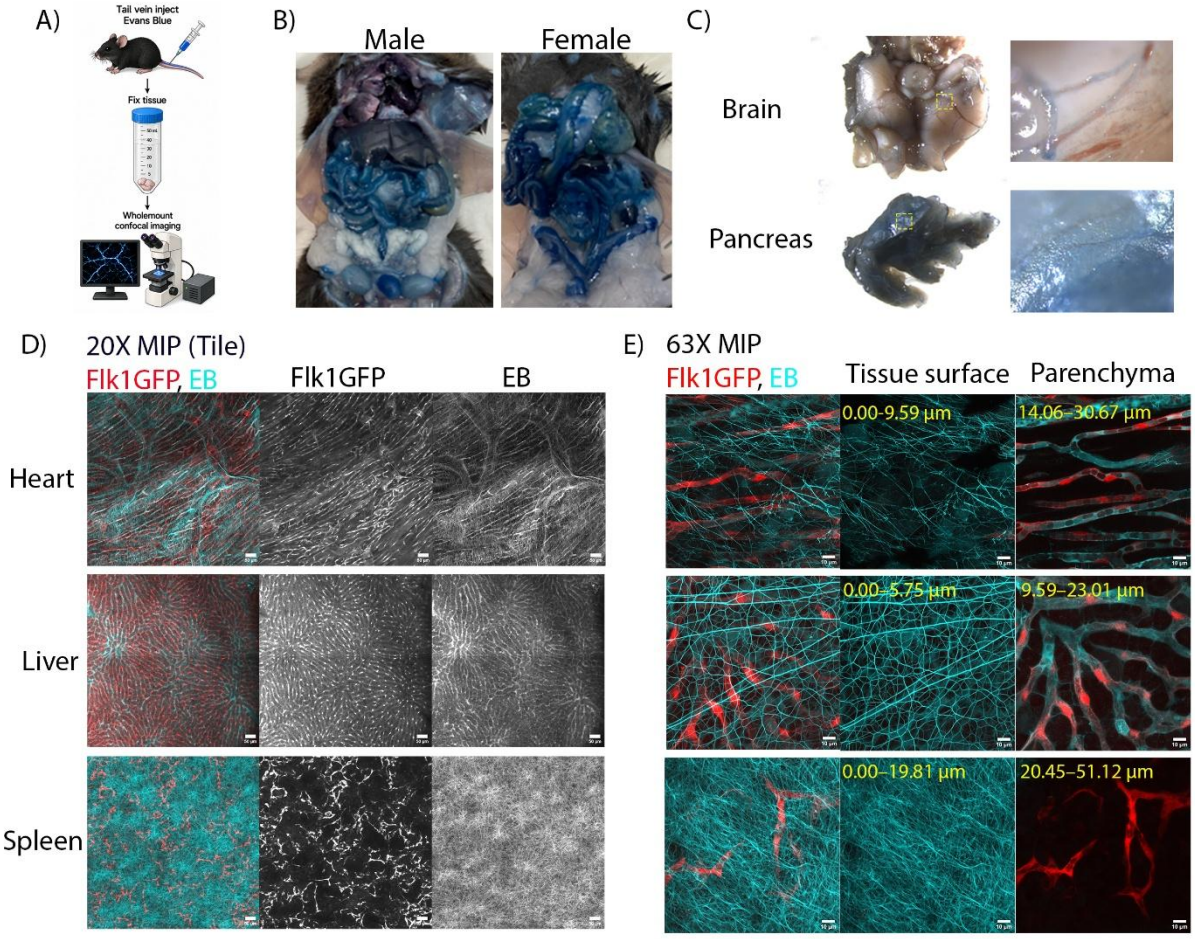


Fig 1: Evans Blue fluorescently labels fibrous structures at tissue surface. (A) Experimental workflow of EB perfusion and wholemount confocal imaging. (B) Gross imaging of EB permeability across visceral organs of male and female mice following tail-vein perfusion, illustrate that the fat, abdominal wall and seminal vesicles remain white in colour whilst other organs exhibit differing degrees of blueness. (C) Gross

brightfield imaging of brain and pancreas following EB perfusion, illustrates containment of EB within vasculature, which contrasts with the pancreas, where EB is observed within interstitium. (D) Low magnification confocal MIPs of visceral organs illustrate visualization of EB fluorescence within Flk1GFP+ vasculature, except for spleen. Scale bar = 50μm (E) High magnification imaging reveals resolved presence of EB fibrous fluorescence at the tissue surface of visceral organs, contrasting with the organ parenchyma, whereby EB fluorescence localizes within the lumen of Flk1GFP capillaries, except for spleen. Scale bar = 10μm.

Evans Blue fibrous fluorescence and fluorescent labelling of arterial elastic membrane is independent of albumin binding.

We wondered whether the EB+ fibrous fluorescence was secondary to albumin binding of the tissue structures, as EB has been suggested to become fluorescent when bound to albumin protein[10,11]. Thus, we co-injected TRITC-albumin with EB and investigated the degree of overlap between their fluorescent signals. We found that despite TRITC-albumin being detected within the Flk1GFP+ capillary lumen and interstitium across organs, the EB-labelled fibrous structures were not co-labelled with TRITC-albumin (Fig 2A). Interestingly, within an arteriole of the brain, we observed that TRITC-albumin remained within the lumen of arterial vasculature, whilst EB labelled the arterioles fibrous elastic membrane. Adjacent Flk1GFP+ vasculature, morphologically resembling a venule with nuclear enrichment of GFP, was not labelled by either signal (Fig 2D). We also performed co-injection of the dyes via IP injection and permitted a longer time for circulation following injection, as we believed this could more accurately reflect the

basal state of physiological fluid flow between capillaries and interstitium. TRITC-albumin labelled cellular populations within the interstitium, providing further evidence that despite TRITC-albumin's extravasation, it did not co-label the EB+ fibrous structures (Sup Fig 1). Co-immunostaining with albumin protein on organ sections further illustrated distinct fluorescent patterns between albumin and EB. EB specifically labelled the internal and external elastic lamellae membrane of the arterial system across organs, while albumin protein was found within the vascular lumen and/or interstitium (Fig 2B). This suggested that free EB, not albumin, was binding to and fluorescently labelling extracellular fibrous structures and the arterial elastic membrane.

The recent advancement of different tissue clearing techniques, in conjunction with EB perfusion and light sheet microscopy, has permitted wholemount visualization of murine vasculature across organ systems and model organisms[10,11]. These studies suggested that EB became fluorescent upon binding albumin within the plasma of intact vasculature, but we wondered whether some of the signal could be derived from binding the arterial elastic membrane. Within the cleared ovarian fat pad, EB+ vasculature exclusively localized adjacent to phalloidin+ circumferential cells that morphologically resembled smooth muscle cells of the arterial system, contrasting with the phalloidin- venous system running parallel to it (Fig 2C). Within cleared brain and kidney tissue EB labelled the elastic membrane of the arterial system, as well as plasma within the lumen of capillaries and/or venules (Fig 2E, Sup Video 1, 2, &3). Utilizing the Fire LUT tool on ImageJ, we visualized that EB, following TV injection and clearing, fluoresced with greater intensity when labelling the arterial elastic membrane than when labelling the plasma localized within the lumen of capillaries and venules

(Fig 2E, Sup Video 1, 2 & 3). We also assessed EB's ability to be used as a stain to label elastic fibres of sectioned aorta tissue derived from WT and *Fbn1*$^{mgR/mgR}$ mice (a mouse model of Marfan syndrome expressing only ~25% of normal fibrillin-1)[17]. EB staining reproduced the typical deficient aortic wall elastic lamellae characterized by frequent breaks in the *Fbn1*$^{mgR/mgR}$ compared to WT mice (Fig 2F)[18]. Thus, EB can be utilized as an alternative cost-effective and convenient method for labelling arterial elastic lamellae.

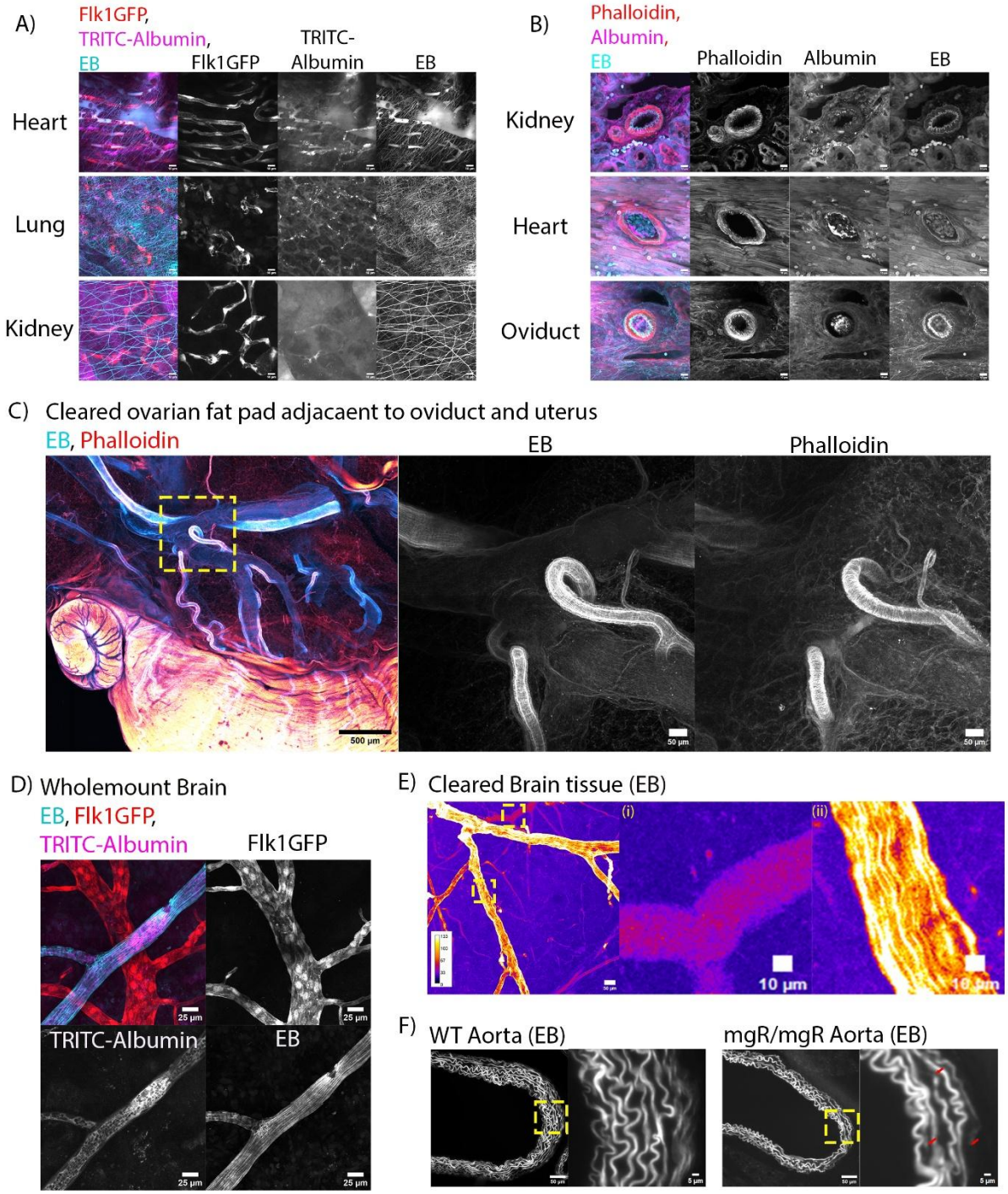


Fig 2: EB fluorescent labelling of fibrous structures and arterial system is independent of albumin binding. (A) Wholemount imaging of visceral organs following EB and TRITC-Albumin co-perfusion within Flk1GFP GEMM illustrates that TRITC-albumin does not co-label EB+ fibrous fluorescence. Scale bar = 10µm. (B) Albumin, phalloidin and EB immunostaining of sectioned visceral organs illustrate that EB labels

arterial elastic membrane, contrasting with albumin. Scale bar = 10μm. (C) Cleared ovarian fat pad following EB perfusion and phalloidin staining illustrates presence of phalloidin+ smooth muscle cells in between EB fluorescence, contrasting with adjacent phalloidin- venous system. Scale bar = 500μm for 10x overview. Scale bar = 50μm for 20x close-up. (D) Wholemount imaging of brain following EB and TRITC-albumin co-perfusion within Flk1GFP GEMM, illustrates non-overlap between EB+ arterial membrane fluorescence and TRITC-albumin's luminal fluorescence. (E) EB fluorescence within the cleared brain displayed using Fire LUT, illustrates warmer colours representing greater fluorescence intensity. (i) EB fluorescence from within vascular lumen. (ii) EB fluorescence derived from arterial system's elastic membrane. (F) EB fluorescent labelling of aorta elastic membrane from WT and *Fbn1*$^{mgR/mgR}$ mice. Red arrows indicate elastic fibre break points within *Fbn1*$^{mgR/mgR}$ aortic wall sections. Throughout, yellow dashed boxes indicate regions shown at higher magnification.

Evans Blue fluoresces when bound to the elastin core of elastic fibres.

Based on EB's ability to fluorescently label the elastic membrane of the arterial system, we speculated that EB binds to elastin, the core of elastic fibres. Elastic fibres consist of an elastin core, comprised of polymerized tropo-elastin (TE), and a surrounding sheath-like structure, comprised of fibrillin-1 (FBN1) microfibrils. We performed EB staining with immunostaining against FBN1 and TE. FBN1 immunostaining did not directly overlap with EB fluorescence and instead labelled the outline of the EB+ fibrous structures (Fig 3A, Video 4). On the other hand, TE immunostaining co-localized with EB+ fibrous structures across murine organs (Fig 3B). To further confirm whether EB

becomes fluorescent when bound to elastin, we mixed EB with commercially available purified elastin protein, derived from bovine neck ligament. No fared fluorescence was observed with EB alone, whilst when mixed with purified elastin bovine ligament (EBL), the fluorescence became visible within the ligaments, suggesting that elastin binding causes EB to fluoresce in the far-red spectrum (Fig 3C).

Considering EB fluorescently labelled elastin independent of albumin, we next investigated whether the fluorescent properties of EB following elastin or albumin binding differed from each other. Interestingly, fluorescent spectral analysis of EB-EBL (elastin) fluorescence illustrated excitation and emission maxima at 640nm and 660nm, respectively, whilst EB-BSA (albumin) fluorescence exhibited the respective maxima at 620nm and 650nm (Sup Fig 2A & B). In addition, FLIM phasor analysis revealed distinct fluorescence decay signatures of EB–EBL and EB–BSA fluorescence. When EB-EBL and EB-BSA were combined *in vitro*, two distinguishable fluorescence populations were observed in phasor space (Sup Fig 2C). These distinct phasor signatures enabled artificial separation and pseudo coloring of EB–EBL and EB–BSA fluorescence (Sup. Fig 2D).

Interestingly, our whole-mount imaging of visceral organ surfaces, including organs not considered elastic, showed that a high density of elastic fibres occurred directly below the mesothelium, while little-to-no elastic fibres were detected within the parenchyma (Fig 1E). To confirm this observation, we used standard 2D section with FBN1 and TE immunostaining. In agreement with our 3D analysis, we found that a high density of elastic fibres localized at the sub-mesothelial layer, with little to no elastic fibres within the organ parenchyma, except for within and around arterial vasculature and within the

lung's parenchyma (Fig 3E, Sup Fig 3, Sup Video 5). The organ surface view of the sub-mesothelial elastic fibres revealed that organ-specific networks differ in fibre density, arrangement and thickness, of which was difficult to elucidate from 2D sections. From the organ surface view, the spleen had the densest network of EB+ elastic fibres within the sub-mesothelial layer, which was found to be significantly greater than the pancreas and liver's network (Fig 3F & 5A). The median diameter of the EB+ elastic fibres ranged from 0.6 to 1.2uM across organs, in agreement with current knowledge (Fig 3G). Interestingly, the elastic fibres in the heart had a significantly thinner diameter than the fibres in lung and spleen, whilst no other significant differences were observed between organs (Fig 3G).

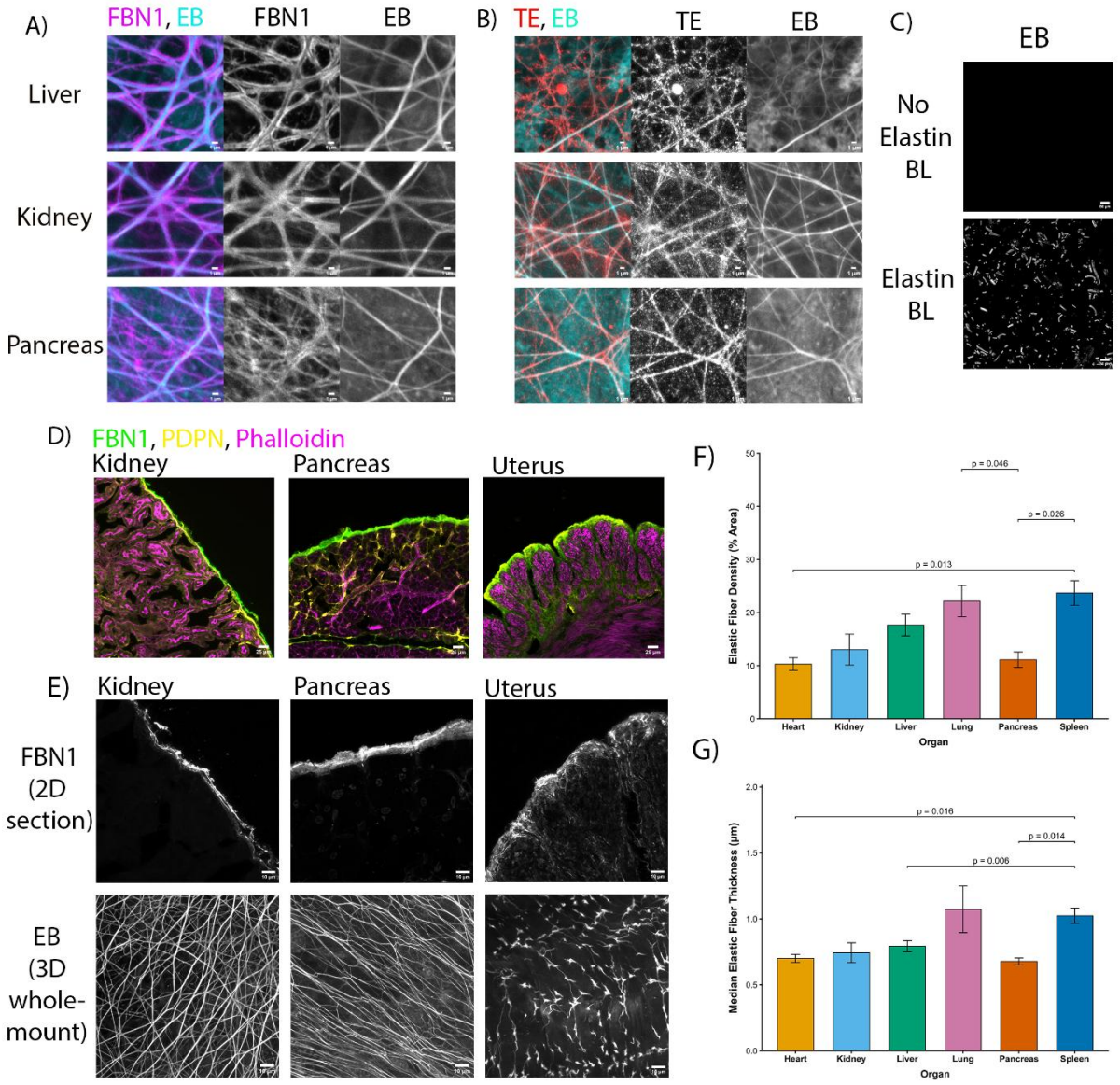


Fig 3: EB becomes fluorescent when bound to tropo-elastin core of elastic fibres.

(A) FBN1and EB wholemount immunostaining of visceral organs illustrates that FBN1 labels the fibre outline whilst EB labels the core. Scale bar = 1µm. (B) TE and EB wholemount immunostaining of visceral organs illustrates co-labelling of elastin core. Scale bar = 1µm. (C) *In vitro* EB fluorescence with and without purified elastin bovine ligament illustrates that EB becomes fluorescent when bound to elastin. Scale bar = 50µm. (D) FBN1, PDPN, and phalloidin immunostaining of cryo-sectioned visceral organs illustrates localization of elastic fibres within mesothelial layer of visceral

organs. Scale bar = 25μm. (E) Contrast between visualizing elastic fibres by FBN1+ cryosection immunostaining and 3D wholemount imaging following EB incubation *ex vivo*. Scale bar = 10μm. (F–G) Sub-mesothelial elastic fibre density and thickness across adult organs. Bars represent mean ± SEM. (F) EB+ elastic fibre density was quantified as EB-positive elastic fibre area relative to total tissue area. (G) Median elastic fibre thickness was measured across the same organs. Technical replicates (2-3 per mouse) were averaged to obtain a mean value for each biological replicate (n = 3-4 per organ). Overall differences among organs were assessed using repeated-measures one-way ANOVA, with p-values provided on graph of any significant differences found between organs comparison ($p < 0.05$).

Evans Blue is an optimal dye for live imaging elastic fibres.

Visualization of elastic fibres is possible with 2-Photon excitation (2PE) microscopy across live and/or fixed tissue through elastin's auto-fluorescence[19,20]. However, auto-fluorescence of other molecules and accessibility to 2-photon microscopy, limit the application of this technique. We wondered whether EB could be a useful live dye for visualizing elastic fibres in *ex vivo* whole-mount tissue. To compare their signal-to-noise ratio, we performed sequential imaging of elastic fibres by 2PE and EB, in conjunction with SHG to label collagen. Although SHG robustly visualized the sub-mesothelial collagen, 2PE of elastic fibres had a low signal-to-noise ratio (Fig 4A), with apparent autofluorescence of other structures. On the other hand, EB strongly labelled the sub-mesothelial elastic fibres with a high signal-to-noise ratio across the different organs

tested without signs of bleaching (Fig 4A). These results suggest that EB is a convenient and cost-effective method for labeling elastic fibres within live tissue.

Recently, several fluorescent dyes have been reported to label ECM structures in live and/or fixed wholemount specimens, such as Rhobo6 and Fastgreen (FG), respectively[21,22]. We first assessed EB's ability to fluorescently label elastic fibres in conjunction with Rhobo6, a novel ECM dye that becomes fluorescent upon glycan binding within live tissue (Fig 4B). Interestingly, despite microfibril associated glycoproteins being a constituent of the elastic fibre, Rhobo6 and EB exhibited mutually exclusive fluorescent patterns in live, non-fixed samples. Rhobo6 labelled wave-like, thicker sub-mesothelial fibrous structures, suggestive of collagen, whilst EB specifically labelled the sub-mesothelial elastic fibres (Sup Fig 4A & B).

Fastgreen (FG) has illustrated its utility to robustly label collagen within the context of large cleared, dehydrated tissue despite having a preference for labelling elastic fibres within hydrated tissue[22]. Interestingly, we found that if tissue was first dehydrated through methanol fixation, and then subsequently treated with EB, within anhydrous conditions, the dye robustly labelled collagen and elastic fibres, illustrating similar patterns to FG (Fig 4C). It is worth noting that the elastin-specific fluorescent signal from EB found in aqueous conditions was not affected by dehydration during clearing procedures (Fig 2C, Sup Video 4). We also assessed FG's ability to label elastic fibres within live *ex vivo* tissue, with Rhobo6. Despite FG labelling sub-mesothelial elastic fibres across live organs, we found that the dye also lightly labelled collagen and some other cellular components (Fig 4D). Thus, EB is uniquely and specifically labelling elastic fibres in contrast with other currently available ECM dyes (Fig 4B & D).

Table 1: Labelling of sub-mesothelial ECM with commercially available dyes.

	EB	**Rhobo6**	**FG**
Live	Elastic fibres.	Glycan ECM (collagen, fibronectin, laminin, aggrecan).	Elastic fibres and collagen.
4% PFA fixation and then treated with dye.	Elastic fibres.	N/A	Elastic fibres and collagen.
Methanol fixation and then treated with dye. (Anhydrous)	Elastic fibres and collagen.	N/A	Elastic fibres and collagen.

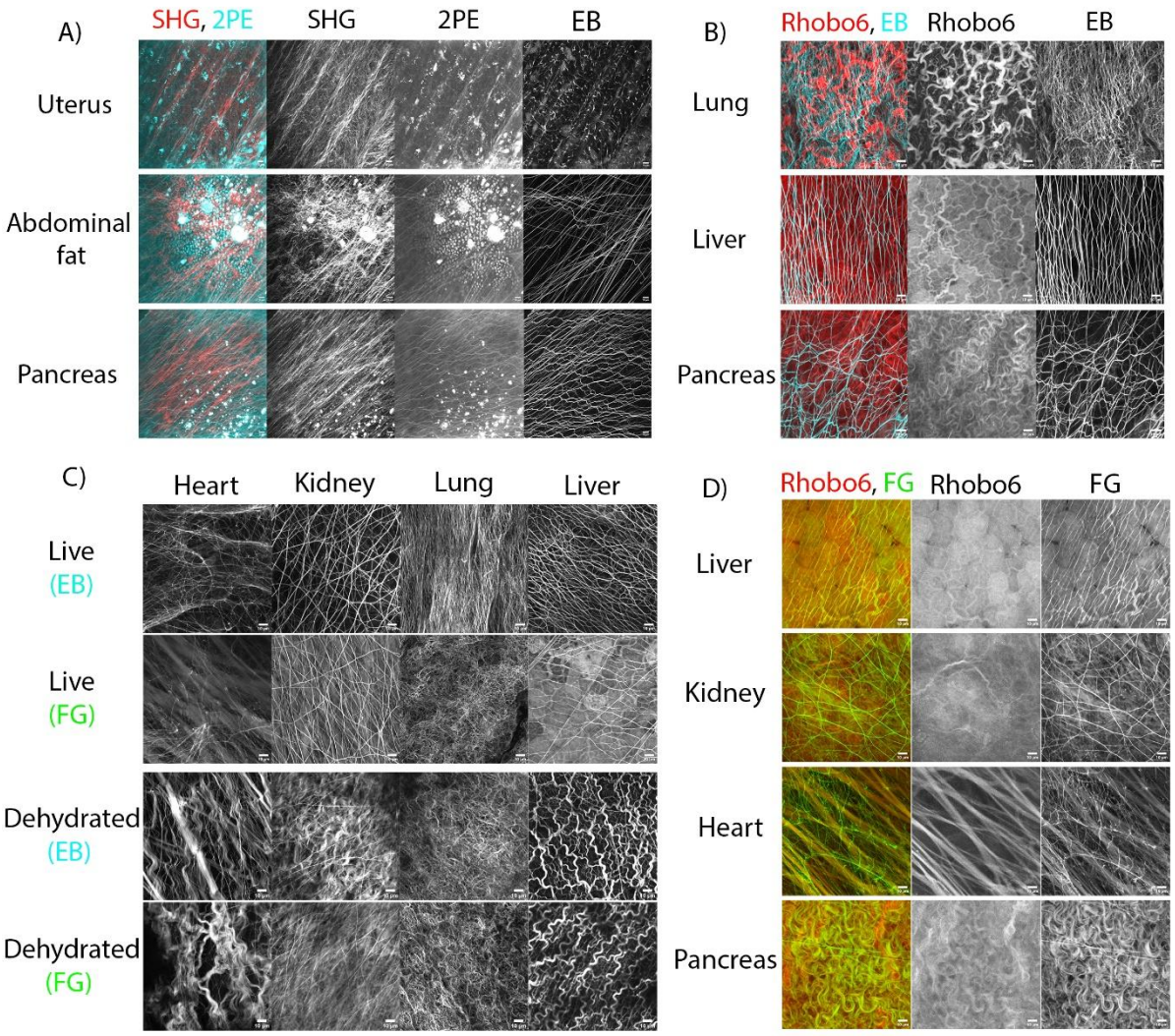


Fig 4: Live imaging of elastic fibres with EB. (A) Wholemount live imaging of collagen and elastic fibres with SHG and 2PE, respectively. EB+ elastic fibres were sequentially imaged in far-red channel illustrating stronger labelling of elastic fibers than 2PE. Scale bar = 10µm. (B) Live *ex vivo* imaging of organs following 1hr incubation with Rhobo6 and EB in vitro, illustrates mutually exclusive patterning of sub-mesothelial ECMs. Scale bar = 10µm. (C) Comparing EB and FG's ability to label elastic fibres within *ex vivo* live tissue and methanol fixed tissue (anhydrous), illustrates that EB more specifically labels elastic fibers in live, hydrated tissue than FG, whilst both dyes robustly label collagen and elastic fibers within anhydrous conditions. Scale bar = 10µm. (D) Live *ex-vivo*

imaging of organs following 1hr incubation with Rhobo6 and FG *in vitro*, illustrates overlap between Rhobo6 and FG structures, resembling collagen. Scale bar = 10μm.

Dynamic changes of the sub-mesothelial ECM across murine lifespan

It is currently suggested that bio-mechanical forces, imposed by the ECM, are partly responsible for regulating organ size and shape, through the process of mechano-transduction[23-25]. In addition, it is suggested that age-associated elastic fibre degradation and/or their dysfunction contributes towards sclerosis of aged tissues[4,5]. However, the involvement of the sub-mesothelial ECM has remained understudied and underappreciated across organ systems and model organisms, especially within 3D contexts[26]. Co-staining of the sub-mesothelial ECM with EB and Rhobo6 allowed visualization of compositional and structural changes at distinct murine life-stages across various live organs (Fig 5).

In P0-P1 neonates, the Rhobo6+ ECM fibres were diffusely labelled and less structurally defined across all organs (Fig 5A). EB also labelled additional fibrous structures within the neonate liver and heart, that were Rhobo6- but based on their 3D structure and width more likely resemble collagen, than elastic fibres (Fig 5A). We observed the reproducible presence of EB+ punctuated foci across neonate organs, likely reflecting the accumulation of extracellular elastin globules prior to the assembly of elastic fibres, during elastogenesis (Sup Fig 5). Interestingly, the EB foci were also found at the periphery of cells, similar to previously defined elastin globule behaviour in tissue culture (Sup Fig 5)[27,28].

From neonate to puberty, the density of sub-mesothelial EB+ elastic fibres, significantly increased across most organs. No significant increase was found between prepubertal and adult mice, suggesting the early maturation and deposition of elastic fibres within mice. On the other hand, the density of sub-mesothelial EB+ elastic fibres decreased across aged organs, whereby a statistically significant difference was observed within the heart and liver (Fig 5A & B). Although, on average, an age-associated decline in elastic fibre density was observed across organs, the high variability, particularly between aged mice, limited statistical significance (Sup Fig 6). A non-significant difference in the median EB+ elastic fibre diameter was observed between adult and aged mice (Fig 5C). We found that differences in elastic fibre density between adult and aged mice, were visible from the 3D surface view but difficult to appreciate from 2D sections. This emphasizes the importance of visualizing the surface view of elastic fibres to elucidate the consequences of an age-related loss of elasticity (Fig 5A, Sup Fig 7).

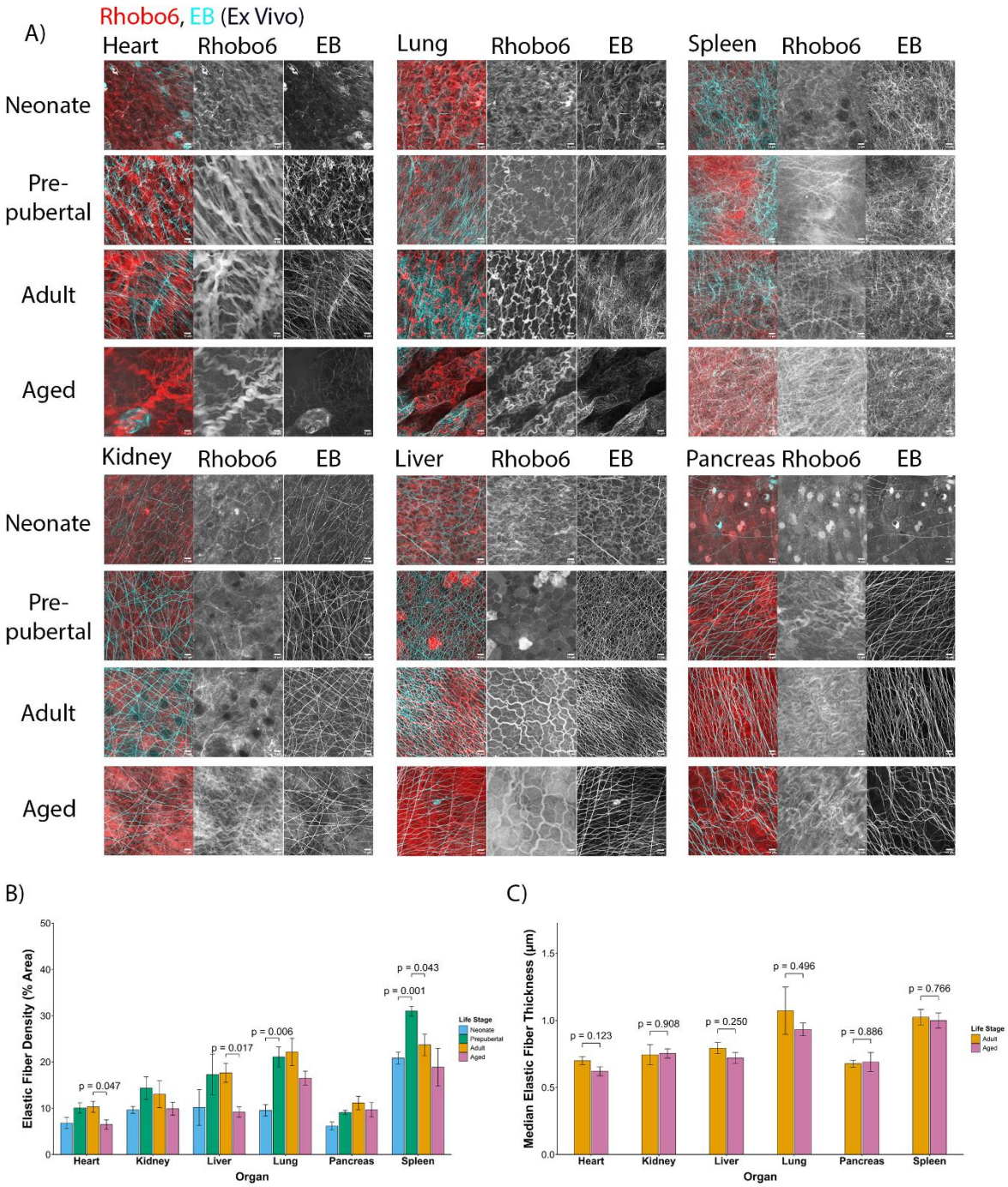


Fig 5: Sub-mesothelial elastic fibres across murine life stages. (A) Representative whole-mount Rhobo6 and EB *ex vivo* live imaging illustrating dynamic changes to sub-mesothelial ECM patterning across different murine life stages. Scale bar = 10µm (B) Quantification of sub-mesothelial EB+ elastic fibre density (% area) across visceral organs at the indicated life stages illustrates an increase in density between neonate

and prepubertal staging and a decrease in density between adult and aged samples. (C) Quantification of EB+ elastic fibre diameter in adult and aged mice across visceral organs. (B-C) Bars represent mean ± SEM; n = 4–5 biological replicates per life stage, with 2–3 technical replicates that were averaged per organ. Statistical comparisons were performed between consecutive life stages (neonate vs. prepubertal, prepubertal vs. adult, and adult vs. aged) using unpaired two-tailed t-tests unadjusted for multiple comparisons. For panel B, significant p-values ($p<0.05$) are indicated on graph. For panel C, non-significant p-values ($p>0.05$) are indicated on graph.

Discussion:

EB has been used for decades to study the permeability of blood vessels, particularly within the brain, whereby leakage of the dye into the interstitium, indicated by its blue colour, has been a useful method to evaluate the integrity of the BBB[6,7]. In addition, EB can fluoresce in the far-red spectrum upon binding to albumin[8,9]. This property has permitted EB to not only be used as a macroscopic visual aid for plasma leakage, but as an albumin tracker that can be used to visualize intact vasculature with laser microscopy across model organisms and tissue[10,11]. Herein, we demonstrated that EB fluoresces upon binding to the core of elastic fibres, elastin, which distributes within compliant, elastic tissues, such as the highly elastic arterial system and lung parenchyma, and in addition, the sub-mesothelium of visceral organs, even those not traditionally considered elastic.

A few classic biochemical studies have suggested that EB has a capacity to bind to tissue components, such as elastin and collagen, in highly elastic organs such as the

aorta and lung[14,15,29]. There is one modern paper that suggests EB fluoresces upon binding elastic fibres, however this was not fully confirmed[30]. We originally suspected that the EB+ fibrous fluorescence following perfusion could be indirect signal due to albumin binding the structures; however, this was not the case because there was no overlap with co-perfused TRITC-albumin. In addition, the distinct spectral and fluorescent lifetime properties of EB upon binding elastin versus albumin, demonstrate that the local molecular environment substantially influences EB's photophysical behaviour. Thus, these differences provide a means to separate fluorescence derived from EB-elastin in comparison to EB-albumin complexes. Across cleared organs, EB was found to robustly label the arterial elastic membrane, whilst weaker fluorescence within less elastic capillaries and venous system likely reflected EB bound to albumin within the blood plasma (Fig 2E). Thus, when utilizing tissue clearing and low-objective light-sheet imaging, EB perfusion may preferentially visualize the elastic arterial system rather than each organ's entire vascular system.

Co-staining with FBN1 and TE immunostaining revealed that the EB+ fibrous structures were elastic fibres. EB and TE labelled the core, whilst FBN1 labelled the fiber's sheath (Fig 3A & B). In addition, we showed that EB becomes fluorescent upon binding purified elastin powder derived from bovine neck ligament. Previously, visualization of elastic fibres has been primarily limited to 2D histological sectioning by classical Verhoeff-Von Gieson staining and/or 3D scanning electron microscopy[31-35], whilst wholemount immunostaining, although possible, has remained notoriously difficult due to epitope masking[30,36-38]. Although 2PE has been shown to visualize elastic fibres in live 3D contexts, its signal-to-noise ratio is low. On the other hand, we found EB to be a

convenient, cheap tool to robustly visualize elastic fibres across live and fixed wholemount tissue.

In addition, we found that this technique worked well with Rhobo6, a novel live glycan ECM dye, that strongly labelled other constituents of the sub-mesothelial ECM such as collagen fibres. Despite reports from classical studies illustrating a widespread presence of elastic fibres within the sub-mesothelial ECM across various tissues and organs[31,33-35,39,40], modern analysis of elastic fibre maturation and aging has been limited to elastic tissues such as the heart, lung, skin and aorta[3-5]. Our visceral organ analysis showed the presence of a high-density of elastic fibres directly below the mesothelium, of which were excluded from the parenchyma – except for the lung and heart. We found that these sub-mesothelial elastic fibres undergo substantial structural and compositional change during organ maturation and with aging. The increased elastic fibre density and complexity found at prepubertal staging, in comparison to the neonatal stage, is suggestive of organ growth saturation and the onset of tensional homeostasis. In addition, we observed a decrease in sub-mesothelial elastic fibre density between adult and aged mice. Since visceral organs are hung and supported by the mesothelium in the peritoneal cavity, their elastic property is required to support their own weight, deformation and smooth movement within the peritoneum. In addition, these sub-mesothelial elastic fibres could exert continuous compressive force on the parenchyma and interstitial fluid within each organ. It is thus likely that it could counteract the internal pressure caused by fluid accumulation and support drainage of interstitial fluid. We envision that the reduction of sub-mesothelial elastic fibres during aging likely results in compromised compressive forces, leading to a disruption to homeostatic fluid drainage and tissue tensegrity[41,42]. The loss of elastic

fibres is thought to cause compensatory collagen production, leading to sclerosis of aged tissue. This age-related change of biomechanical forces likely causes or at least influences, altered cellular behaviour during the aging process, resulting in chronic disease development such as cardiovascular disease and/or cancer[43,44].

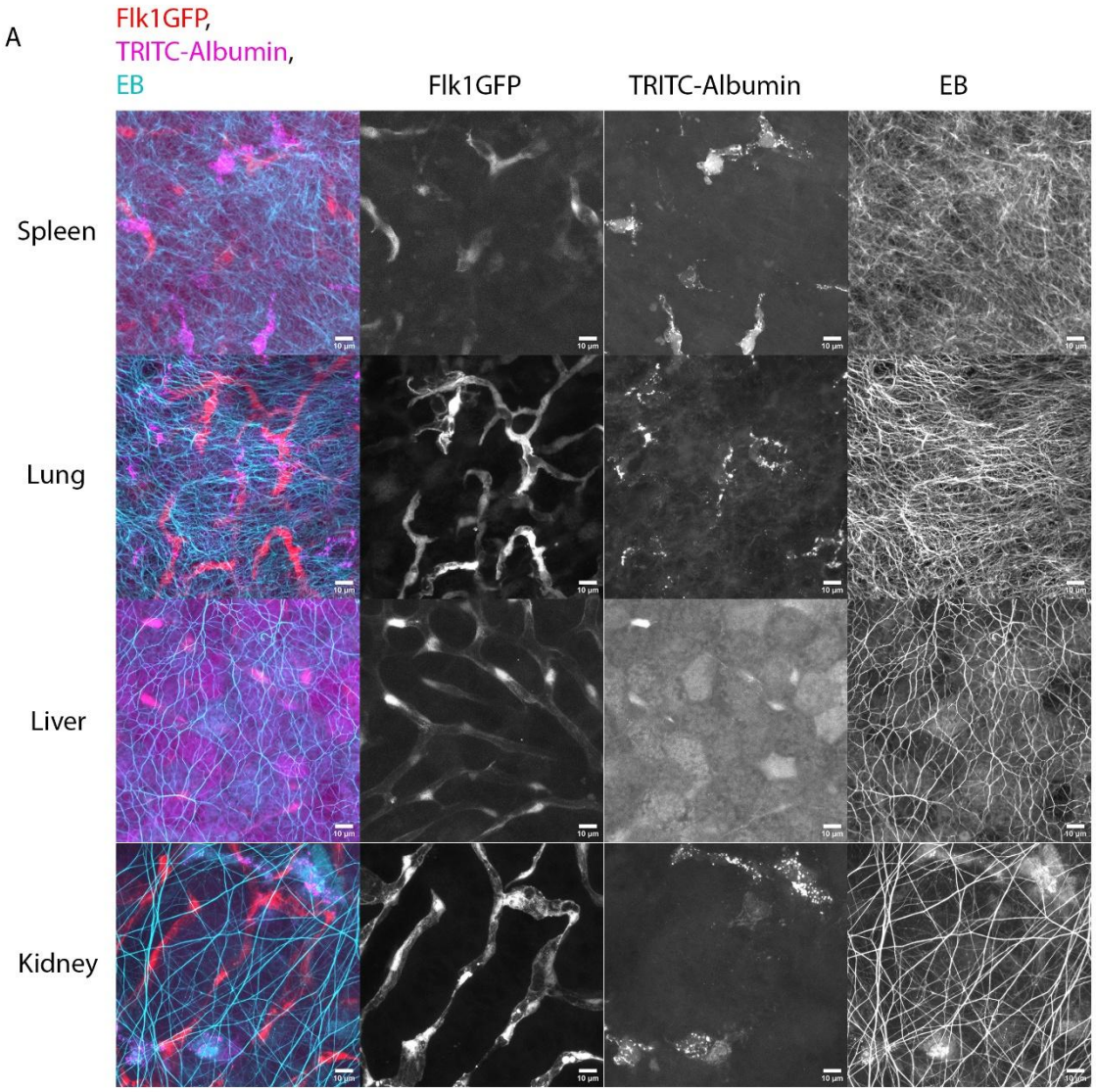
In conclusion, EB is a highly reproducible and robust method for visualizing elastic fibres. Its unique ability to label elastic fibres across 3D contexts of live, fixed and/or cleared wholemount tissue in a timeless and cost-effective manner, provides unprecedented opportunities to gain insight into their physiological role across development, organ maturation and homeostasis, and how their loss during the aging process may act as a critical vulnerability towards chronic disease development and/or mortality.

Limitations:

Although EB staining of elastic fibres overlapped with TE immunostaining, whether direct binding of TE is responsible for its fluorescence, or whether the dye binds indirectly through another protein unit, remains unknown and awaits further biochemical validation. We recognized the local variation of elastin network density in the submesothelial layer of organs/tissues. This reflects local variation in mechanical stress in organs/tissues, resulting in variation in age-associated degradation. Future high-resolution whole-organ scanning would provide more detail on local variation of organ mechanics and identify potential weak hinge points.

Acknowledgements: Images were collected and/or image processing and analysis for this manuscript was performed in the McGill University Advanced BioImaging Facility (ABIF), (RRID:SCR_017697). We would like to specifically thank Dr Joel Ryan for helping perform the fluorescent spectral and FLIM analysis of EB fluorescence upon albumin and elastin binding. We would like to thank Nobuko Yamanaka for mouse colony maintenance. This study was financially supported by the Canadian Institute of Health Research (CIHR) project grants (PJT180446 to YY, PJT190288 to KC) and by the Natural Sciences and Engineering Research Council of Canada (RGPIN-2022-05045 to DPR). K.C. is a Tier 2 Canada Research Chair in Dynamics of Tissue Regeneration. The study was also financial supported by the following awards: CRRD Trainee Fellowship Award, R&M Gosselin Grad Studentship Award, Clifford Pang Aging Science Doctoral Scholars Award (WP).

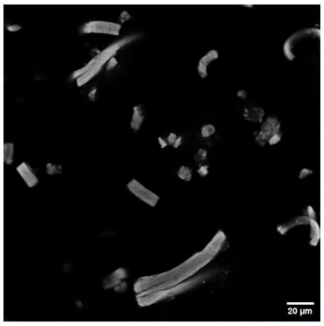
Supplementary data:

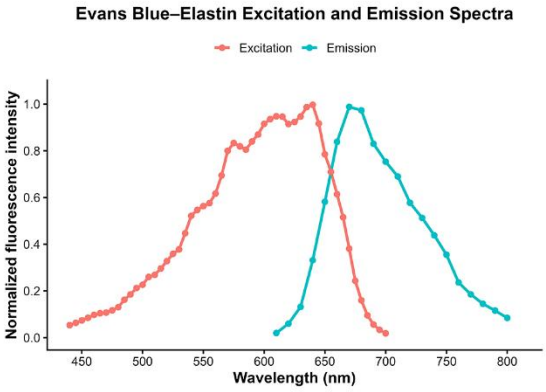


Sup Fig 1: IP injected TRITC-albumin and EB do not overlap, despite presence of TRITC-albumin within interstitium. The TRITC-Albumin signal following IP injection, does not localize within Flk1GFP vasculature but rather within interstitium, visualized as puncti within the spleen, lung and kidney, and as diffuse signal within the liver. In contrast, the EB signal robustly labels fibrous structures present within interstitium. Scale bar = 10μm.

A)

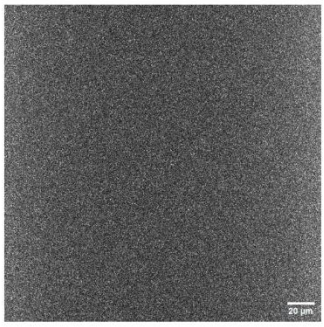
EB + EBL

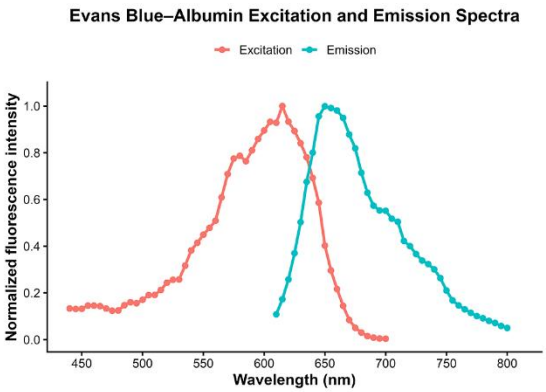




B)

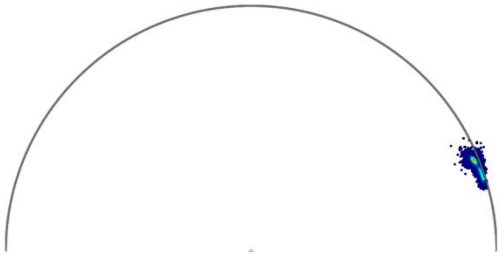
EB + BSA





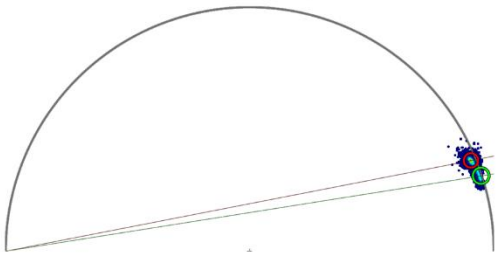
C)

FLIM Phasor plot

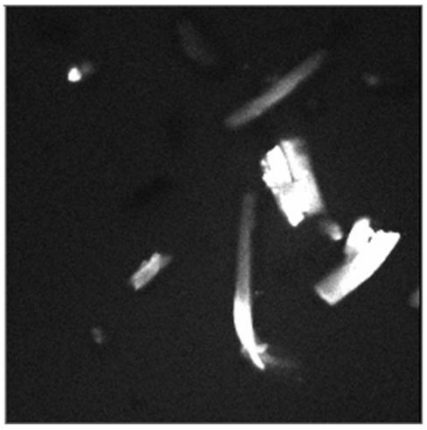


D)

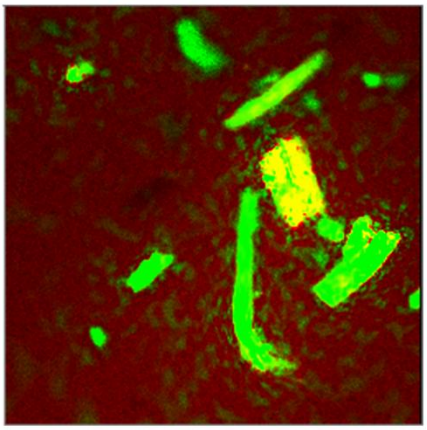
FLIM Phasor plot



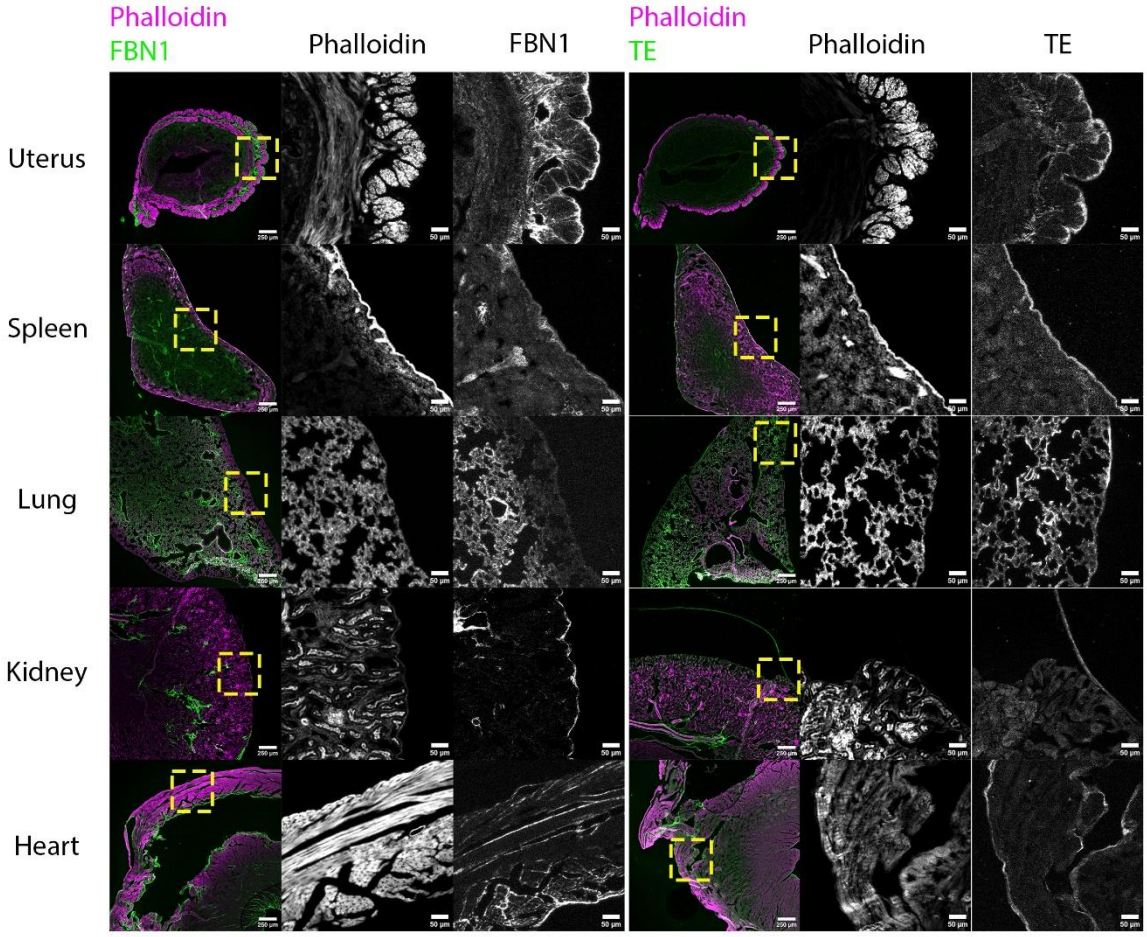
EB-EBL + EB-BSA



Artificial separation of EB-EBL & EB-BSA fluorescence

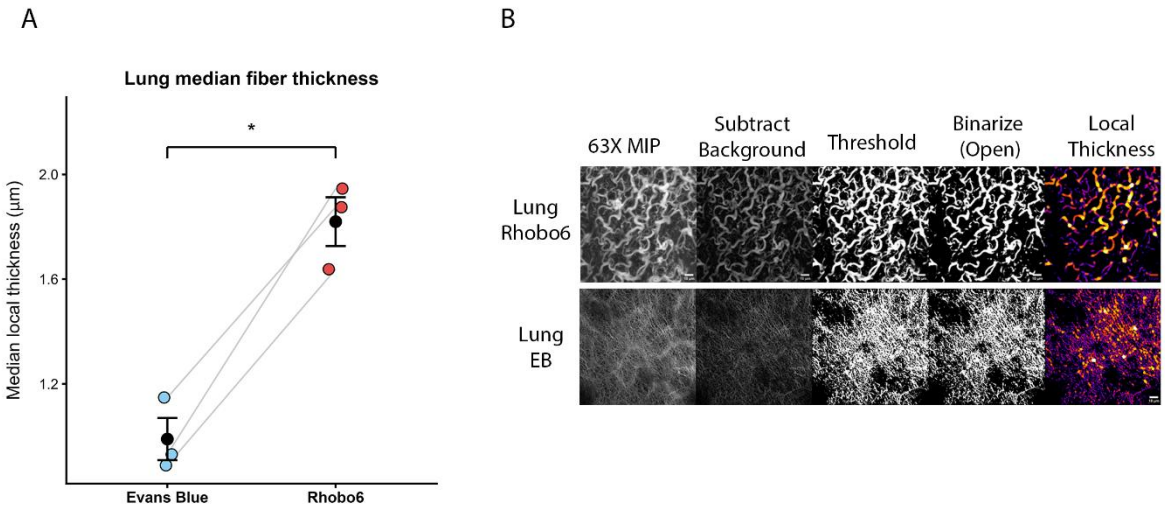


Sup Fig 2: EB-EBL (elastin) and EB-BSA (albumin) complexes have distinct photophysical properties. (A) The fluorescent spectra of the EB-EBL (elastin bovine ligament) complex illustrate excitation and emission peaks of 640nm and 660nm, respectively. Scale bar = 20µm. (B) In contrast, EB-BSA (bovine serum albumin) have respective peaks at 620nm and 650nm. Scale bar = 20µm. (C) FLIM phasor plot of EB-EBL mixed with EB-BSA illustrates two distinguishable fluorescence populations in phasor space. (D) Artificial separation and pseudo coloring of EB-EBL and EB-BSA fluorescence based on distinct phasor signatures.

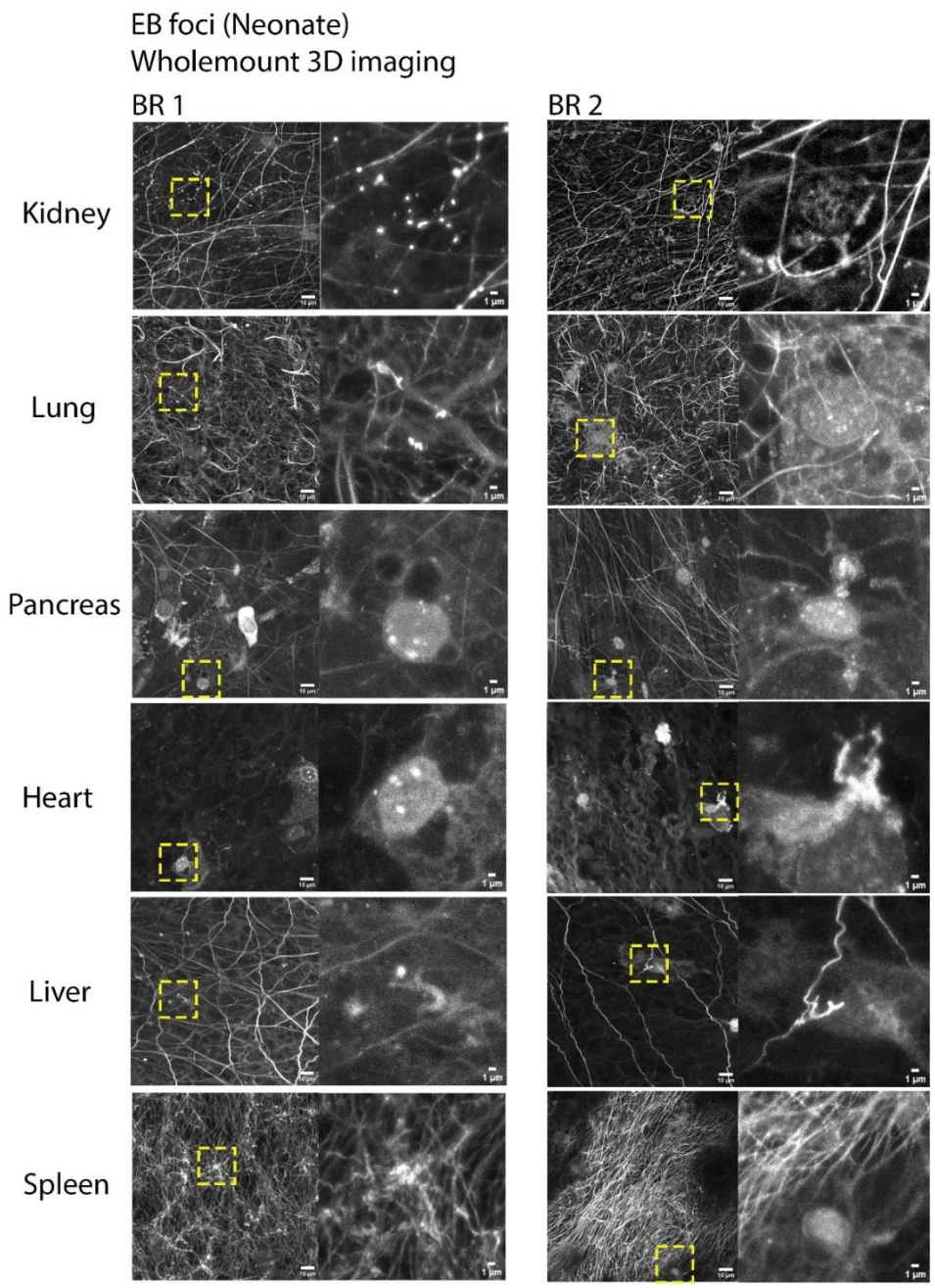


Sup Fig 3: FBN1 and TE localize at tissue periphery across visceral organs. FBN1 and TE immunostaining of visceral organ cryosections illustrate that a dense localization of

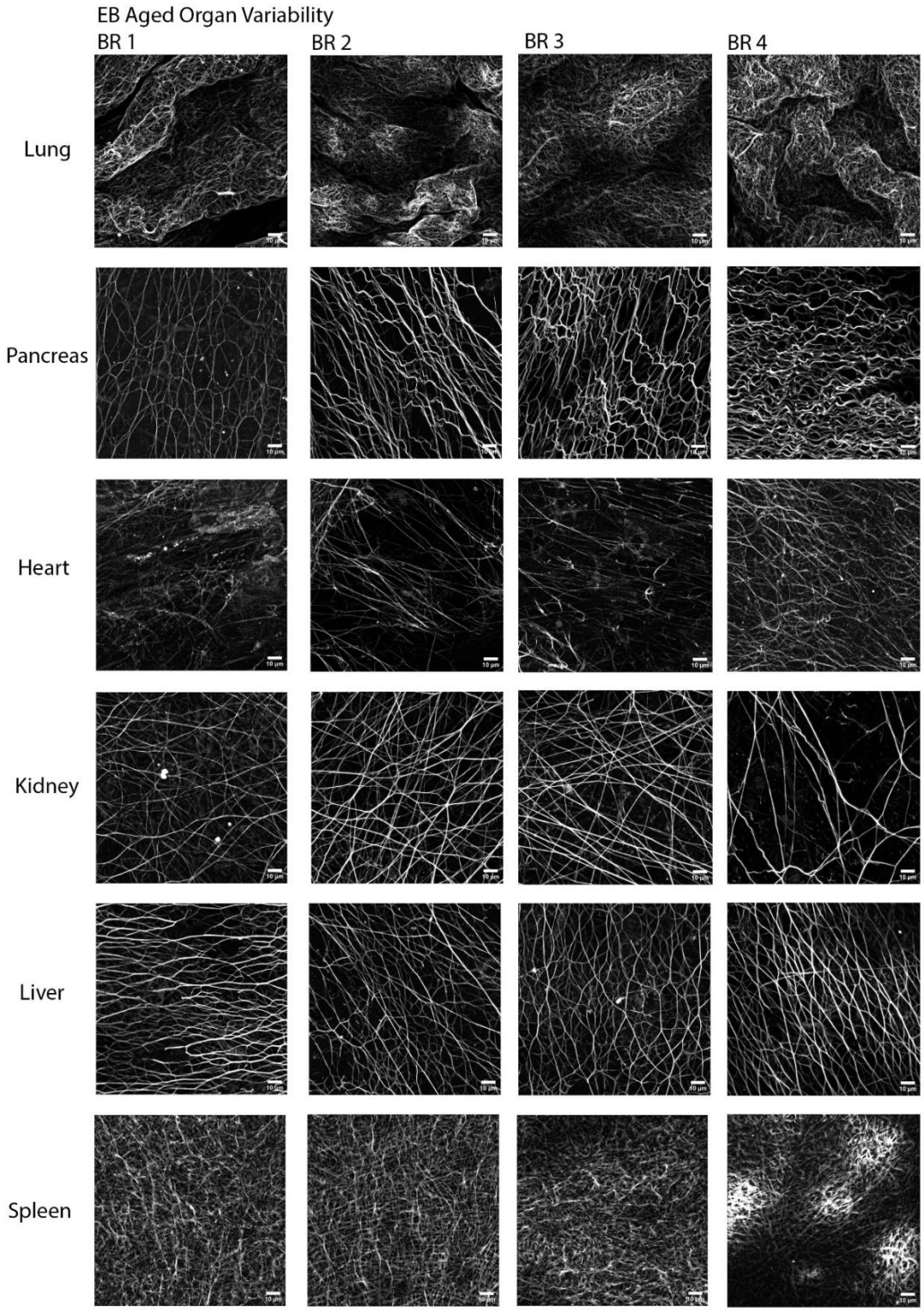
elastic fibers occurs at organ surface. Scale bar = 200μm for section overview. Scale bar = 50μm for magnified regions using ImageJ optical zoom.



Sup Fig 4: EB and Rhobo6 median local thickness quantification scheme within the lung. (A) The median local thickness of lung surface Rhobo6+ fibres is significantly greater than EB+ elastic fibers. (B) The sequential image processing utilized to quantify the median local thickness of fibers with ImageJ. Scale bar = 10μm.

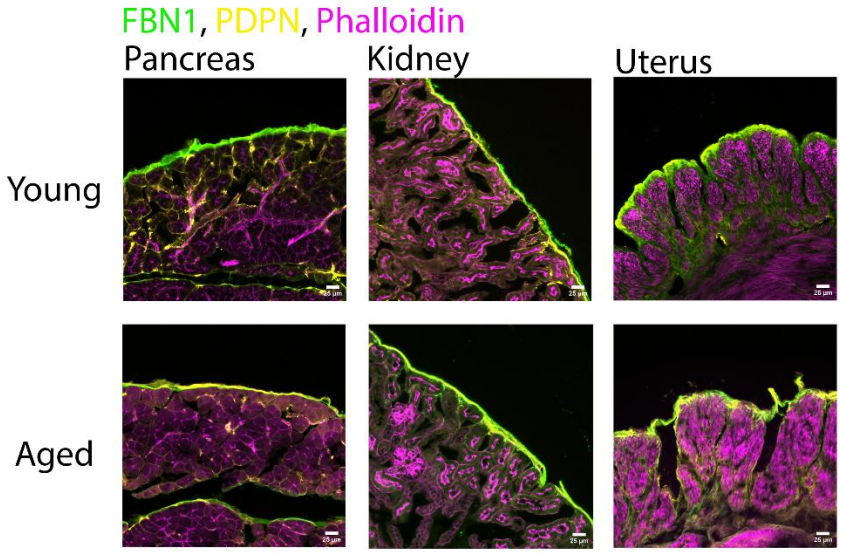


Sup Fig 5: Wholemount imaging of neonate organs reveals presence of EB foci and nascent fibrous elongation at cell periphery. EB foci localizing at cellular periphery likely resemble organization of elastin globules during nascent elastogenesis at the neonate organ surface. Scale bar = 10µm for 63x MIP overview. Scale bar = 1µm for magnified regions (yellow boxes) using ImageJ optical zoom.



Sup Fig 6: Variability of sub-mesothelial EB+ elastic fibre density and organization across biological replicates of aged organs. A MIP of each aged biological replicate is illustrated to emphasize the biological variability that was observed amongst aged

organs. Certain aged organs reflect greater elastic fiber disruption than others within the context of one aged animal. Scale bar = 10µm.



Sup Fig 7: Limited differences in sub-mesothelial elastic fibre density or organization can be elucidated from 2D perspective between young and aged visceral organs. FBN1 Immunostaining of young and aged organ cryosections illustrates that limited differences in elastic fibre organization and/or density can be realized by 2D perspective. Scale bar = 25µm.

Methods:

Intravenous perfusion:

200µl of 1% EB (w/v) (Sigma Aldrich, E2129) was tail-vein injected into 2–5-month-old Flk1GFP mice that were restrained using tail-vein restrainer. Mice were subsequently moved to cage whereby 15 minutes of circulation was permitted before the mice were

euthanized via cervical dislocation. Organs were immediately dissected and fixed in 4% PFA (PFA, Polysciences) overnight at 4 °C. Organs were washed with PBS (PBS, BioShop Canada Inc., PBS405) before imaging wholemount within Ibidi µ Slide 8 well^{High} (Ibidi, 80826) and/or Matek glass bottom dishes (Matek, P35G-1.5-20-C). 100µl of PBS was pipetted into each well before placing an organ into each chamber. The organ's surface that was closest to the glass bottom dish and thus microscope, was imaged.

For co-perfusion experiment, 100ul of TRITC-Albumin (25mg/ml) (Invitrogen, A23016) and 100µl of 1% EB (10mg/ml) were co-injected via the tail-vein as described directly above. Subsequent steps taken were performed as described directly above.

Vibratome sectioning and staining:

Mice were euthanized via cervical dislocation, and organs were immediately dissected and fixed in 4% PFA overnight. Organs were washed with PBS three times, 15 min each. The organs were placed in a cryomold and embedded in around 1ml of warmed 4% low melting agarose (LMA) (IBI Scientific, IB70051). The solidified LMA block was super-glued onto metal specimen holder. Tissue was vibratome sectioned into 150µm sections. The slices were picked up using a paintbrush and placed in a well with 24 well plate containing permeabilization and blocking solution (0.1% Triton X (TX) (Sigma-Aldrich, T8787), 0.5% Fish Gelatin stock (Sigma Aldrich, G7765). Tissue sections were permeabilized and blocked overnight. The following day, primary antibody staining was performed within permeabilization and blocking solution and left overnight (anti-albumin (Abcam, EPR20195) (1:500)). The following day the sections were washed with PBS, then 0.1% Tween (Sigma Aldrich, P9416), and again with PBS. Following the washes, secondary antibody staining was performed within PBS (1:500) and was left

overnight (AF 555 anti-rabbit (Invitrogen, A31572), AF-405 Phalloidin (Invitrogen, A30104)). The next day, the same wash procedure was performed. The sections were then transferred to a #1.5 coverslip with a 120µm spacer stuck to the surface. A second coverslip was then placed on top, before imaging the sections with LSM710 confocal microscope.

Wholemount staining and tissue clearing:

Mice were perfused and fixed as described above. Tissue was permeabilized overnight with 1% TX diluted within PBS, before being treated with Phalloidin overnight. Wholemount organs were cleared according to their original published protocols for FluoClearBABB, FDISCO, and EZ-Clear protocols with some minor adjustments. For both FDISCO and EZ -Clear protocols the pH of the THF was not adjusted with triethylamine. For imaging of the FluoClearBABB tissue, the organs were placed within BABB solution in between silicone spacers that were stuck on top of a glass coverslip. For imaging of the EZ-Clear and FDISCO cleared tissue, organs were imaged in their clearing solutions within a Matek glass bottom dish.

Image processing:

ImageJ (FIJI) was utilized to create maximum projections of Z-stacks taken with LSM710 confocal microscope. ImageJ fire tool was utilized to show signal differences between EB+ arterial and venule lumen fluorescence. IMARIS's animation tool was utilized to create 3D videos of cleared organs.

Wholemount antibody immunostaining:

Mice were euthanized as described above. Organs were immediately dissected fixed for 2 hours in 4% PFA. Organs were permeabilized and blocked overnight within 0.1%TX and 1% FBS diluted with PBS. The following day, primary antibody staining was performed within the permeabilization and blocking solution (1:500) (anti-TE (Generation described in PMID 30036393), anti-FBN1(Generation described in PMID:33039488), anti-PDPN (Thermo Fisher, 14-5381-82)). 48 hours later, PBS washes were performed on each organ. Secondary antibody staining was performed in PBS (1:500) for 24 hours, of which was followed by multiple PBS washes (AF anti-rabbit 488 (Invitrogen, A21206), AF-405 Phalloidin (Invitrogen, A30104) and 1% EB. The organs were then imaged wholemount within an Ibidi 8 µ-well chamber (Ibidi, 80826) and/or Matek glass bottom chamber as described above.

Cryo-sectioning and immunostaining of cryosections:

Organs were fixed for 3 hours with 4% PFA on shaker. Organs were washed in PBS and then left within PBS overnight in 4°C fridge. The organs were then dehydrated using a sucrose gradient, 10% for 2 hours, 20% for 2 hours, and 30% overnight. Organs were cut in half transversely and embedded in OCT. The moulds were then stored in -80°C freezer. Organs were cryo-sectioned into 10µm sections using cryostat. Tissue sections were equilibrated to room temperature and rehydrated with PBS. Sections were permeabilized with TX using sequential incubations in 0.1% TX, 0.5% TX and again with 0.1% TX. Sections were subsequently blocked at room temperature in PBS containing 0.1% Triton X-100 and 0.5% fish gelatin. Primary antibodies were diluted in blocking solution (1:250), applied to the sections, covered with parafilm, and incubated overnight at 4°C (anti-TE (Generation described in PMID 30036393), anti-

FBN1(Generation described in PMID:33039488), anti-PDPN (Thermo Fisher, 14-5381-82). The following day, sections were washed with PBS, followed by washes with 0.1% Tween and washes with PBS. Sections were then incubated overnight at 4°C with the appropriate fluorescent secondary antibodies (1:450) diluted in PBS (AF anti-rabbit 488 (Invitrogen, A21206), AF anti-hamster 546 (Invitrogen, A-21111), AF-405 Phalloidin (Invitrogen, A30104). Sections were washed three times with PBS, three times with 0.1% Tween, and three times with PBS. Slides were mounted with mounting medium and #1.5 coverslips on top, which was subsequently sealed with nail polish, and stored at 4°C until imaging.

SHG and 2PE wholemount live imaging:

Organs were excised and transferred to 5ml of physiological saline solution containing EB (50µg/ml). Organs were live imaged using a 2-Photon LSM 880 confocal microscope. The organs were first imaged using the multi-photon mode. Tissue was excited at 860nm, whereby backward SHG was detected within the 400-500nm wavelength range, while auto-fluorescent elastic fibres were detected within the 500-600nm wavelength range. Following the multi-photon imaging, we used the conventional confocal modality to sequentially image the same region of each organ, whereby EB was excited within the Far-Red (647nm) spectrum. Images were acquired with a Zeiss LSM880NLO microscope equipped with a Chameleon Discovery NX multiphoton laser (Coherent) using a 63x oil immersion lens (Zeiss, NA:1.0).

Wholemount Rhobo6 and EB in vitro staining of ex vivo organs:

Neonate mice were euthanized by decapitation, whilst other life stages were euthanized by cervical dislocation. Organs were dissected from mice and transferred to 5ml tube

containing Rhobo6 (3.78µg/ml) and EB (50µg/ml) dissolved within physiological saline. The organs were incubated for 1 hour, before wholemount live imaging within an Ibidi 8 µ-well chamber as described above. Each organ surface that was imaged was the region of the organ that was found closest to the microscope. 2-3 technical replicates were performed and averaged to provide one biological replicate per organ. n = 3-4 mice were used for each life-stage.

Comparative wholemount staining of ECM between FG and EB:

For *ex vivo* live imaging, mice were euthanized by cervical dislocation before dissection of organs. The organs were then placed in either FG solution (100µg/ml) or EB solution (50µg/ml) within a 5ml Eppendorf and placed on shaker for 1 hour. Organs were then imaged wholemount as described above.

For dehydrated fixed imaging, mice were euthanized and organs dissected as described above. The organs were then immediately fixed in 100% methanol overnight. The following day the organs were then placed in FG (2µg/ml) or EB (50µg/ml) diluted within methanol.

Mouse aorta preparation:

The preparation of aortae from WT and *Fbn1*$^{mgR/mgR}$ mice followed previously described procedures[18,45].

Fluorescent spectral analysis and FLIM:

Fluorescence spectral and fluorescence lifetime imaging microscopy (FLIM) analyses of Evans Blue (EB) associated with elastin or albumin were performed using a Leica STELLARIS 8 confocal microscope equipped with a tunable pulsed while-light laser,

photon counting detection, and FALCON software for FLIM analysis, using a HC PL APO CS2 20x 0.75 air objective. For EB–EBL measurements, 10µl of 1% (w/v) EB was mixed with 2 ml of powdered elastin bovine ligament (EBL). For EB–albumin measurements, 10µl of 1% (w/v) EB was mixed with 2ml of 50% bovine serum albumin (BSA). Samples were imaged separately for fluorescence spectral characterization. Excitation spectra were acquired by sequentially varying the excitation wavelength from 440-700nm in 5nm increments. Emission spectra were acquired over the 600-810nm detection range using 20nm spectral detection windows, with 10nm steps for EB–EBL and 5nm steps for EB–BSA. Five regions of interest (ROIs) were selected for each sample, and mean fluorescence intensity was quantified at each spectral position. For spectral analysis, fluorescence intensities within each ROI were normalized to the maximum intensity of the corresponding spectrum and subsequently averaged across the five ROIs to generate normalized excitation and emission profiles. For FLIM analysis, the EB–EBL and EB–BSA samples were combined and imaged using the STELLARIS 8 FLIM acquisition system. Fluorescence decay characteristics were assessed by phasor analysis, and the resulting differences in phasor distributions were used to distinguish EB–EBL from EB–BSA associated fluorescence. These populations were subsequently pseudo colored to enable artificial separation and visualization of EB–EBL and EB–BSA fluorescence within the mixed sample.

EB elastic fibre density quantification:

Elastic fibre density was quantified from whole-mount CZI image stacks using Fiji/ImageJ. For each image stack, a maximum-intensity projection was first generated across the z-stack. Background fluorescence was removed using the Subtract

Background function with a rolling-ball radius of 50 pixels. Following background subtraction, images were converted to binary masks using the ImageJ Default automatic thresholding method. To reduce small, grain-like features and isolated foreground pixels, the resulting binary images were processed using Binary Open. Elastic fibre density was subsequently quantified as the percentage of the analysed image area occupied by the threshold EB-positive signal (% area). The same automated image-processing parameters were applied to all images to minimize variability introduced by manual threshold selection. 2-3 technical replicates were analysed for each organ from each biological replicate. Technical replicate measurements were averaged to generate a single elastic fibre density value for each organ within each biological replicate. These biological-replicate means were used for subsequent statistical analyses and comparisons across organs and life stages.

EB elastic fibre diameter quantification:

Elastic fibre thickness was quantified from confocal image stacks using a custom batch-processing macro in Fiji/ImageJ. For each image, a maximum-intensity projection was generated from the Z-stack. Background fluorescence was removed using the rolling-ball background subtraction algorithm with a radius of 50 pixels. Images were subsequently segmented using Fiji's Default automatic thresholding method and converted to binary masks. The binary open operation was then applied to reduce small foreground artifacts and refine the segmented fiber mask. Local elastic fiber thickness was then determined using the Local Thickness (masked, calibrated, silent) algorithm, which calculates local thickness based on the diameter of the largest sphere that fits within the segmented structure while preserving the spatial calibration of the original

images. Background pixels with zero local thickness were excluded from quantitative analysis. The median, minimum, maximum, and mean local thickness, as well as the standard deviation, were calculated for each image. The median local thickness per image was used as the primary measure of elastic fiber thickness for subsequent comparisons between samples.

Video generation:

Videos were generated with IMARIS 11.1 using ABIFs licence at McGill university.

References:

1 Walma, D. A. C. & Yamada, K. M. The extracellular matrix in development. *Development* **147**, doi:10.1242/dev.175596 (2020).

2 Frantz, C., Stewart, K. M. & Weaver, V. M. The extracellular matrix at a glance. *Journal of Cell Science* **123**, 4195-4200, doi:10.1242/jcs.023820 (2010).

3 Schmelzer, C. E. H. & Duca, L. Elastic fibers: formation, function, and fate during aging and disease. *The FEBS Journal* **289**, 3704-3730, doi:https://doi.org/10.1111/febs.15899 (2022).

4 Heinz, A. Elastic fibers during aging and disease. *Ageing Research Reviews* **66**, 101255, doi:https://doi.org/10.1016/j.arr.2021.101255 (2021).

5 Sherratt, M. J. Tissue elasticity and the ageing elastic fibre. *Age (Dordr)* **31**, 305-325, doi:10.1007/s11357-009-9103-6 (2009).

6 Goldim, M. P. d. S., Della Giustina, A. & Petronilho, F. Using Evans Blue Dye to Determine Blood-Brain Barrier Integrity in Rodents. *Current Protocols in Immunology* **126**, e83, doi:https://doi.org/10.1002/cpim.83 (2019).

7 Saunders, N. R., Dziegielewska, K. M., Møllgård, K. & Habgood, M. D. Markers for blood-brain barrier integrity: how appropriate is Evans blue in the twenty-first century and what are the alternatives? *Frontiers in Neuroscience* **Volume 9 - 2015**, doi:10.3389/fnins.2015.00385 (2015).

8 Saria, A. & Lundberg, J. M. Evans blue fluorescence: quantitative and morphological evaluation of vascular permeability in animal tissues. *Journal of Neuroscience Methods* **8**, 41-49, doi:https://doi.org/10.1016/0165-0270(83)90050-X (1983).

9 Namykin, A. A., Khorovodov, A. P., Semyachkina-Glushkovskaya, O. V., Tuchin, V. V. & Fedosov, I. V. Photoinduced Enhancement of Evans Blue Dye Fluorescence in Water Solution of Albumin. *Optics and Spectroscopy* **126**, 554-559, doi:10.1134/S0030400X19050217 (2019).

10 Honeycutt, S. E. & O'Brien, L. L. Injection of Evans blue dye to fluorescently label and image intact vasculature. *Biotechniques* **70**, 181-185, doi:10.2144/btn-2020-0152 (2021).

11 Hsu, C.-W. *et al.* EZ Clear for simple, rapid, and robust mouse whole organ clearing. *eLife* **11**, e77419, doi:10.7554/eLife.77419 (2022).
12 Allen, T. H. & Orahovats, P. D. Combination of toluidine dye isomers with plasma albumin. *Am J Physiol* **161**, 473-482, doi:10.1152/ajplegacy.1950.161.3.473 (1950).
13 Rawson, R. A. THE BINDING OF T-1824 AND STRUCTURALLY RELATED DIAZO DYES BY THE PLASMA PROTEINS. *American Journal of Physiology-Legacy Content* **138**, 708-717, doi:10.1152/ajplegacy.1943.138.5.708 (1943).
14 Lindner, V. & Heinle, H. Binding properties of circulating evans blue in rabbits as determined by disc electrophoresis. *Atherosclerosis* **43**, 417-422, doi:https://doi.org/10.1016/0021-9150(82)90040-5 (1982).
15 Dallal, M. M. & Chang, S. W. Evans blue dye in the assessment of permeability-surface area product in perfused rat lungs. *J Appl Physiol (1985)* **77**, 1030-1035, doi:10.1152/jappl.1994.77.2.1030 (1994).
16 Steiniger, B. S., Pfeffer, H., Gaffling, S. & Lobachev, O. The human splenic microcirculation is entirely open as shown by 3D models in virtual reality. *Scientific Reports* **12**, 16487, doi:10.1038/s41598-022-19885-z (2022).
17 Pereira, L. *et al.* Pathogenetic sequence for aneurysm revealed in mice underexpressing fibrillin-1. *Proc Natl Acad Sci U S A* **96**, 3819-3823, doi:10.1073/pnas.96.7.3819 (1999).
18 Zhang, R. M. *et al.* Fibrillin-1-regulated miR-122 has a critical role in thoracic aortic aneurysm formation. *Cell Mol Life Sci* **79**, 314, doi:10.1007/s00018-022-04337-8 (2022).
19 Mansfield, J. *et al.* The elastin network: its relationship with collagen and cells in articular cartilage as visualized by multiphoton microscopy. *J Anat* **215**, 682-691, doi:10.1111/j.1469-7580.2009.01149.x (2009).
20 König, K., Schenke-Layland, K., Riemann, I. & Stock, U. A. Multiphoton autofluorescence imaging of intratissue elastic fibers. *Biomaterials* **26**, 495-500, doi:https://doi.org/10.1016/j.biomaterials.2004.02.059 (2005).
21 Fiore, A. *et al.* Live imaging of the extracellular matrix with a glycan-binding fluorophore. *Nature Methods* **22**, 1070-1080, doi:10.1038/s41592-024-02590-2 (2025).
22 Timin, G. & Milinkovitch, M. C. High-resolution confocal and light-sheet imaging of collagen 3D network architecture in very large samples. *iScience* **26**, 106452, doi:https://doi.org/10.1016/j.isci.2023.106452 (2023).
23 Eder, D., Aegerter, C. & Basler, K. Forces controlling organ growth and size. *Mechanisms of Development* **144**, 53-61, doi:https://doi.org/10.1016/j.mod.2016.11.005 (2017).
24 Mim, M. S. *et al.* Piezo regulates epithelial topology and promotes precision in organ size control. *Cell Rep* **43**, 114398, doi:10.1016/j.celrep.2024.114398 (2024).
25 Mori, Y. *et al.* A self-limiting mechanotransduction feedback loop ensures robust organ formation. *bioRxiv*, 2025.2009.2025.678607, doi:10.1101/2025.09.25.678607 (2025).
26 Liu, X. *et al.* Interplay of ECM organization, ROCK signaling, and cell polarity drives mesothelium formation and lung growth. *Nature Communications* **16**, 9610, doi:10.1038/s41467-025-64597-3 (2025).

27 Kozel, B. A. *et al.* Elastic fiber formation: a dynamic view of extracellular matrix assembly using timer reporters. *J Cell Physiol* **207**, 87-96, doi:10.1002/jcp.20546 (2006).
28 Kozel, B. A. & Mecham, R. P. Elastic fiber ultrastructure and assembly. *Matrix Biol* **84**, 31-40, doi:10.1016/j.matbio.2019.10.002 (2019).
29 Heinle, H. & Lindner, V. The binding of Evans blue to collagen and elastin in elastic tissue. *Arch Int Physiol Biochim* **92**, 13-17, doi:10.3109/13813458409073408 (1984).
30 Chaweewannakorn, C. *et al.* Imaging of muscle activity-induced morphometric changes in fibril network of myofascia by two-photon microscopy. *Journal of Anatomy* **238**, 515-526, doi:https://doi.org/10.1111/joa.13339 (2021).
31 Section 3--selected biological properties of tissues: potential determinants of susceptibility to ultrasound-induced bioeffects. American Institute of Ultrasound in Medicine. *J Ultrasound Med* **19**, 85-96, 154-168, doi:10.7863/jum.2000.19.2.85 (2000).
32 Kardon, D. E., Borczuk, A. C. & Factor, S. M. Mechanism of Pericardial Expansion with Cardiac Enlargement. *Cardiovascular Pathology* **9**, 9-15, doi:https://doi.org/10.1016/S1054-8807(99)00029-0 (2000).
33 Kai, T., Nishizono, H. & Kimura, K. Fiber Arrangement of the Rat Splenic Capsule with Special Reference to Elastic Fibers. *Okajimas Folia Anatomica Japonica* **77**, 167-179, doi:10.2535/ofaj1936.77.5_167 (2000).
34 Watanabe, N. & Nishizono, H. A Scanning and Transmission Electron Microscopic Study of Fiber Arrangement in the Hepatic Capsule. *Okajimas Folia Anatomica Japonica* **71**, 279-295, doi:10.2535/ofaj1936.71.5_279 (1994).
35 Knudsen, P. J. The peritoneal elastic lamina. *J Anat* **177**, 41-46 (1991).
36 Shen, Z., Lu, Z., Chhatbar, P. Y., O'Herron, P. & Kara, P. An artery-specific fluorescent dye for studying neurovascular coupling. *Nat Methods* **9**, 273-276, doi:10.1038/nmeth.1857 (2012).
37 Mortimer, G. M. & Minchin, R. F. Cryptic epitopes and functional diversity in extracellular proteins. *The International Journal of Biochemistry & Cell Biology* **81**, 112-120, doi:https://doi.org/10.1016/j.biocel.2016.10.020 (2016).
38 Schenk, S. & Quaranta, V. Tales from the crypt[ic] sites of the extracellular matrix. *Trends in Cell Biology* **13**, 366-375, doi:https://doi.org/10.1016/S0962-8924(03)00129-6 (2003).
39 Michailova, K., Wassilev, W. & Wedel, T. Scanning and transmission electron microscopic study of visceral and parietal peritoneal regions in the rat. *Annals of Anatomy - Anatomischer Anzeiger* **181**, 253-260, doi:https://doi.org/10.1016/S0940-9602(99)80040-5 (1999).
40 Ishihara, T. *et al.* Histologic and ultrastructural features of normal human parietal pericardium. *The American Journal of Cardiology* **46**, 744-753, doi:https://doi.org/10.1016/0002-9149(80)90424-5 (1980).
41 Ingber, D. E. TENSEGRITY: THE ARCHITECTURAL BASIS OF CELLULAR MECHANOTRANSDUCTION. *Annual Review of Physiology* **59**, 575-599, doi:https://doi.org/10.1146/annurev.physiol.59.1.575 (1997).
42 Boghdady, C. M., Kalashnikov, N., Mok, S., McCaffrey, L. & Moraes, C. Revisiting tissue tensegrity: Biomaterial-based approaches to measure forces across length scales. *APL Bioeng* **5**, 041501, doi:10.1063/5.0046093 (2021).

43 Marino, G. E. & Weeraratna, A. T. A glitch in the matrix: Age-dependent changes in the extracellular matrix facilitate common sites of metastasis. *Aging and Cancer* **1**, 19-29, doi:https://doi.org/10.1002/aac2.12013 (2020).
44 Halsey, G., Sinha, D., Dhital, S., Wang, X. & Vyavahare, N. Role of elastic fiber degradation in disease pathogenesis. *Biochim Biophys Acta Mol Basis Dis* **1869**, 166706, doi:10.1016/j.bbadis.2023.166706 (2023).
45 Lau, C., Muthu, M. L., Siddiqui, I. F., Li, L. & Reinhardt, D. P. High-Fat Diet Has a Protective Sex-Dependent Effect on Aortic Aneurysm Severity in a Marfan Syndrome Mouse Model. *Can J Cardiol* **39**, 1553-1567, doi:10.1016/j.cjca.2023.07.020 (2023).